

1 Inflation Experiments and Inverse Finite Element Modelling of Posterior Human
2 Sclera
3

4 Brendan Geraghty^{1*}, Ahmed Abass², Ashkan Eliasy², Stephen W. Jones², Paolo Rama³, Wael
5 Kassem⁴, Riaz Akhtar², Ahmed Elsheikh^{2, 5, 6}

6

7 ¹Department of Musculoskeletal Biology, Institute of Ageing and Chronic Disease, University
8 of Liverpool, L7 8TX, UK

9 ²School of Engineering, University of Liverpool, Liverpool L69 3GH, UK

10 ³Ophthalmology Department, San Raffaele Scientific Institute, Milan, Italy

11 ⁴Division of Construction Engineering, Umm Al-Qura University, College of Engineering at Al-
12 Qunfudah, Al-Qunfudah 21912, Saudi Arabia

13 ⁵National Institute for Health Research (NIHR) Biomedical Research Centre at Moorfields, Eye
14 Hospital NHS Foundation Trust and UCL Institute of Ophthalmology, UK

15 ⁶School of Biological Science and Biomedical Engineering, Beihang University, Beijing, China

16

17 ***Author for correspondence:**

18 Brendan Geraghty, Department of Musculoskeletal Biology, Institute of Ageing and Chronic
19 Disease, University of Liverpool, L7 8TX, UK

20 bren@liverpool.ac.uk

21

22 **Keywords:** human sclera, material properties, numerical simulation, finite element modelling,

24

25 **Financial Disclosure(s):** None of the authors have financial disclosures.

26

27 **Declaration of interest:** None

28

29 **Contributions:**

30 A. Elsheikh designed and supervised the project. PR provided donor specimens. BG carried
31 out the experiments, analysed the data, interpreted results and wrote the manuscript. WK
32 analysed the results. AA analysed the results and edited the manuscript. RA, SJ and A. Eliasy
33 interpreted the results and edited the manuscript. All authors have reviewed the manuscript,
34 approved the final draft and provided a significant contribution to the study.

35

36

37 **Number of words:** 3,723 (excluding in-text citations)

38 **Abstract**

39 The complexity of inverse finite element modelling methods used in ocular biomechanics
40 research has significantly increased in recent years in order to produce material parameters
41 that capture microscale tissue behaviour. This study presents a more accessible method for
42 researchers to optimise sclera material parameters for use in finite element studies where
43 macroscale sclera displacements are required.

44

45 Five human donor sclerae aged between 36 and 72 years were subjected to cycles of internal
46 pressure up to 61mmHg using a custom-built inflation rig. Displacements were measured
47 using a laser beam and two cameras through a digital image correlation algorithm. Specimen-
48 specific finite element models incorporating regional thickness variation and sclera surface
49 topography were divided into six circumferential regions. An inverse finite element procedure
50 was used to optimise Ogden material parameters for each region.

51

52 The maximum root mean squared (RMS) error between the numerical and experimental
53 displacements within individual specimens was 17.5 μm . The optimised material parameters
54 indicate a gradual reduction in material stiffness (as measured by the tangent modulus) from
55 the equator to the posterior region at low-stress levels up to 0.005 MPa. The variation in
56 stiffness between adjacent regions became gradually less apparent and statistically
57 insignificant at higher stresses.

58

59 The study demonstrated how inflation testing combined with inverse modelling could be used
60 to effectively characterise regional material properties capable of reproducing global sclera
61 displacements. The material properties were found to vary between specimens, and it is
62 expected that age could be a contributing factor behind this variation.

63

64 **Introduction**

65 Finite element (FE) modelling has long been recognised as a valuable tool for better
66 understanding ocular response to mechanical actions. Many early studies focused on the
67 cornea, where FE modelling was used to simulate the conditions caused by intraocular
68 pressure (IOP) elevation or experienced in tonometry (Elsheikh and Wang, 2007), impact
69 (Uchio et al., 1999), surgery (Alastrue et al., 2006, Fernandez et al., 2006) and disease (Gefen
70 et al., 2009). Similarly, the behaviour of the sclera, the optic nerve head (ONH) and lamina
71 cribrosa was the subject of several simulation studies due to their importance in the
72 development and progression of glaucoma (Coudrillier et al., 2013, Downs et al., 2003, Eilaghi
73 et al., 2010, Girard et al., 2009b, Girard et al., 2011, Grytz et al., 2014a, Sigal, 2009, Sigal et
74 al., 2005).

75

76 In order to pursue the use of FE modelling as a tool in ophthalmology-related research, the
77 ability to experimentally characterise the biomechanical behaviour of ocular tissues is of
78 primary importance. Of the various test methods used, inflation is considered the most
79 desirable owing to the similarity in loading mode experienced by the tissue when compared to
80 in vivo intraocular pressure. Due to its anisotropic behaviour, complex geometry and variable
81 wall thickness, inverse FE modelling has become an increasingly common method of
82 determining sclera material properties. Since its first application in the field of ocular
83 biomechanics by Woo et al. (1972), the complexity of inverse FE modelling methods have
84 significantly increased. For instance, Girard et al. (2009c) developed an anisotropic
85 hyperelastic constitutive model that predicted preferred collagen fibre orientation. Grytz and
86 Meschke (2010) applied a method that also accounted for collagen crimp while Coudrillier et
87 al. (2013) and Zhou et al. (2019) incorporated wide-angle x-ray scattering (WAXS) data of
88 collagen fibril orientations. These intricate approaches allow for the characterisation of
89 microscale behaviour of the sclera. However, implementation of the necessary processes can

90 be time consuming and the incorporation of collagen distribution data into an FE model
91 requires technical user subroutines that are not always accessible to researchers.

92

93 This study aimed to produce a set of regional Ogden material parameters capable of predicting
94 macroscale deformation behaviour of the sclera. Ex-vivo specimens were tested using a
95 combination of experimental inflation, 2D digital image correlation (DIC) and inverse FE
96 analysis. Specimen-specific FE meshes divided into six circumferential regions, each with an
97 optimised pair of parameters capable of reproducing macroscale sclera displacements, were
98 used in the inverse analysis. This approach accounts for the previously reported anterior to
99 posterior variation in sclera material properties without the need to include detailed
100 microstructure data thereby reducing the time required for data acquisition and post-test
101 analysis. The presented methodology, and its results, can be used in FE studies where
102 macroscale sclera displacements are apt.

103

104 **Materials and Methods**

105 **Specimen Preparation**

106 Five human donor sclerae were obtained fresh from the Fondazione Banca degli Occhi del
107 Veneto, Italy. The average and standard deviation of the donors' age was 61.8 ± 15.6 years
108 (range 36 to 72 years). Routine screening was used to exclude donors with human
109 immunodeficiency virus, hepatitis B and C, syphilis, central nervous system degenerative
110 diseases, active infections, diabetes, eye tumours and glaucoma. The sclerae were not frozen
111 at any stage. Ethical approval to use the specimens in research was obtained by the eye bank
112 in accordance with the Declaration of Helsinki and its revisions up to 2013. The specimens
113 were extracted approximately 6 hours after death, preserved in storage medium Eusol-C
114 (Alchimia, Padova, Italy) and tested within 3 days post mortem. The limit of 3 days was based
115 on the results of a previous experimental study confirming the maintenance of scleral tissue
116 quality in the preservation medium Eusol-C for up to 5 days (Geraghty et al., 2012).

117

118 The sclerae were surgically detached from the cornea, extraocular muscles, retina and
119 choroid. In order to assess if tissue swelling occurred during transit, nine thickness
120 measurements were obtained between the anterior foramen and posterior pole post-
121 enucleation by the eye bank using an UP-1000 ultrasound pachymeter (Nidek, Gamagori,
122 Japan). The superior cardinal point on the anterior foramen edge and the measurement
123 locations were marked using a gentian violet pen, as shown in Figure 1 (a) and (b). The
124 measurements were repeated at the same locations before conducting the tests at the authors'
125 laboratory using a Pachmate 55 (DGH Technologies, Exton, PA) with 5 μm accuracy. The
126 average difference between the two sets of measurements was $4\pm 25 \mu\text{m}$, which is within the
127 range previously reported for a comparison of conventional and handheld pachymeters
128 (Queirós et al., 2007), thereby confirming that tissue swelling did not occur. The sclerae
129 dimensions were measured using an electronic Vernier calliper (D00352, Duratool, Taiwan)
130 with $10\mu\text{m}$ accuracy. The diameter of the anterior foramen after removal of the cornea was
131 $17.75\pm 0.64 \text{ mm}$, the specimen depth from the foramen edge to the posterior pole 19.54 ± 0.45
132 mm and the equatorial diameter $24.26\pm 0.38 \text{ mm}$, as shown in Figure 1 (b).

133

134 The superior, inferior, temporal and nasal (orthogonal) directions and the four 45° and 135°
135 (diagonal) directions were marked on the anterior foramen edge of each specimen. The
136 posterior pole was located by placing the specimens on their anterior foramen and marking
137 the uppermost point on the posterior region. A flexible plastic strip marked with 2 mm
138 increments was extended between the posterior pole and the anterior foramen to provide a
139 guide for thickness measurements at 2 mm intervals along the eight meridians shown in Figure
140 1 (c) and (d). The pachymeter obtained 50 measurements per point and the average value
141 was recorded. The regional thickness variation data obtained from this procedure was utilised
142 in the generation of specimen-specific finite element meshes for the inverse analysis
143 procedure.

144

145 **Inflation testing**

146 The sclerae were anatomically orientated and fixed along their anterior foramen using a
147 specially designed clamping mechanism. The clamps provided a secure grip of the anterior
148 sclera without the need for adhesives, as shown in Figure 2 (a). The clamped sclerae were
149 filled with a saline solution before connection to an inflation test rig which was developed in
150 an earlier study (Elsheikh et al., 2007). The specimens had a thin covering of the preservation
151 medium Eusol-C upon removal from storage which prevented dehydration of the outer surface
152 during testing.

153

154 Each specimen was subject to three cycles of internal pressure change from 1 mmHg up to
155 61 mmHg. Cyclic pressure changes were managed by means of a small reservoir whose
156 vertical movement was computer-controlled and set to a pressure change rate of 37.5
157 mmHg/min. The pressure within the sclera was monitored using a differential pressure
158 transducer (FDW, RDP Electronics, Wolverhampton, UK). Initial trials were carried out to
159 assess the number of cycles required to produce repeatable pressure-displacement behaviour
160 and the resulting tissue stiffness at maximum IOP. A significant difference was observed
161 between the first and second cycle but little difference was observed thereafter. Consequently,
162 the results of the third cycle were considered representative of stable material behaviour.
163 Similar to previous studies on the mechanical properties of the sclera (Coudrillier et al., 2012,
164 Fazio et al., 2012), all tests were carried out at room temperature (21°C).

165

166 **Specimen Imaging**

167 Displacement of the specimens was monitored along the orthogonal (superior-inferior and
168 temporal-nasal) meridians of the sclera using two 14.7 MP digital cameras (Canon, Tokyo,
169 Japan) with 4416 × 3312 pixels per image and orientated as shown in Figure 2 (b). Specimens
170 were connected to the inflation rig ensuring alignment of the temporal-nasal and superior-
171 inferior axes with the orthogonal planes. Prior to testing, a pulverised fuel ash powder was
172 dispersed over the external surface of each sclera to enhance optical contrast. During the third

173 loading cycle, individual images with an accuracy of 12.6 μ m/pixel were taken at pressures of
174 1, 16, 31, 46 and 61mmHg using Remote Capture software (Canon, Tokyo, Japan).

175

176 2D digital image correlation (DIC) software (geoPIV8, Cambridge, UK) was used to analyse
177 successive camera images and determine the movement of points on the sclera surface in
178 the form of 2D displacement vectors measured in pixels. 1D posterior displacements along
179 the ocular longitudinal axis were also continuously monitored using an LK-031 laser
180 displacement sensor (Keyence, Milton Keynes, UK) with 1 μ m accuracy. The laser
181 displacement sensor measurements provided a means of calibrating the DIC software outputs
182 to convert the displacements from pixels to millimetres. The resulting vectors obtained from
183 the 2D DIC analysis were then used to produce pressure-displacement target curves for use
184 in the inverse modelling procedure at the nine points located at 0°, 30° and 60° relative to the
185 longitudinal axis on the superior-inferior and temporal-nasal meridians, as shown in Figure 2
186 (c) and (d).

187

188 **Inverse Modelling Procedure**

189 Sclera material behaviour parameters were derived from the experimental data using HEEDS
190 Professional 5.2 (Red Cedar Technology, Michigan, USA), a design optimisation software, in
191 conjunction with the nonlinear FE software Abaqus (Dassault Systèmes Simulia Corp., Rhode
192 Island, USA). The SHERPA robust optimisation search algorithm, which is embedded in the
193 optimisation software, was used. This algorithm spanned the parameter space while
194 attempting to achieve convergence in targeted regions.

195

196 The FE mesh was generated using a custom written Visual Basic code (Microsoft, Redmond,
197 WA) which utilised a diamatic dome configuration and consisted of one layer of 19661 fifteen-
198 node C3D15H hybrid continuum elements. The FE meshes incorporated specimen-specific
199 outer surface topography and sclera wall thickness variations. Due to the inability to measure
200 the dimensions of the lamina cribrosa, this component was modelled as a group of six

201 elements occupying a circular area with 0.9 mm radius, 0.3 mm thickness, 0.3 MPa Young's
202 modulus and centre located 2.7 mm away from the posterior pole (Saude, 1993, Sigal, 2009).

203

204 Movement of model nodes located on the anterior foramen was restrained in the three main
205 directions, u, v and w, to simulate the conditions created by the mechanical clamps of the
206 inflation rig. All other nodes possessed three degrees of freedom; displacement in u, v and w.

207 Anterior to posterior variation of sclera material behaviour was enabled by dividing the model
208 into 6 regions as illustrated in Figure 3, with region 1 being the most anterior and region 6
209 encompassing the posterior pole. Initial trials found 6 regions to be suitable for the current
210 study as decreasing the number of regions reduced the accuracy of fit between the
211 experimental and numerical results.

212

213 The SHERPA algorithm was used to determine a pair of first-order Ogden material parameters
214 for each sclera region (see Appendix) by minimising the root mean square (RMS_{local}) error
215 between the experimental and numerical posterior displacements at the nine targeted points
216 on the sclera surface using the following objective function for each point where:

$$RMS_{local} = \sqrt{\frac{1}{P} \cdot \sum_{p=1}^P (\delta_p^{exp} - \delta_p^{num})^2} \quad \text{Equation 1}$$

217 where P is the total number of pressure levels at which the RMS is calculated (i.e. 16, 31, 46
218 and 61 mmHg), and δ_p^{exp} and δ_p^{num} represent the orthogonal components of the experimental
219 and numerical displacements for a given point on the sclera surface at pressure level p . The
220 optimisation algorithm also minimised RMS_{total} , the average of the local errors, where:

$$RMS_{total} = \frac{1}{N} \sum_{n=1}^N RMS_{local} \quad \text{Equation 2}$$

221 where N is the total number of selected points on the scleral surface. Nodes in the FE mesh
222 which corresponded to these locations were monitored and the optimisation software adjusted

223 the material parameters of each element group until the best possible fit was achieved
224 between the experimental and numerical pressure-displacement results.

225

226 **Statistical Analysis**

227 The significance of associations between biomechanical properties (tangent modulus) and
228 distance from posterior pole was assessed by Spearman rank correlation. The tests were
229 performed in IBM SPSS Statistics 21 (IBM, Armonk, NY). $P < 0.05$ was considered an indication
230 of statistical significance.

231

232 **Results**

233 **Experimental Results**

234 All sclerae exhibited maximum thickness in the region of the posterior pole with values ranging
235 between 1014 and 1108 μm ($1076 \pm 23 \mu\text{m}$). Thickness reduced progressively up to 6mm away
236 from the posterior pole before reducing more rapidly down to a minimum of between 478 and
237 770 μm ($630 \pm 76 \mu\text{m}$) at 20 mm from the posterior pole. This was then followed by a rapid
238 increase that continued to the edge of the anterior foramen ($757 \pm 59 \mu\text{m}$). Beyond 4-6 mm
239 from the pole, measurements taken along the diagonal meridians exhibited greater thickness
240 than the orthogonal meridians, however, all lines followed the same thickness variation
241 pattern. These values were used to produce contour maps of the thickness variation over a
242 developed scleral surface and the average of all specimens is shown in Figure 4. The maps
243 were realised by creating a Delaunay triangulation between the thickness measurement
244 locations and applying a cubic interpolation function within these regions.

245

246 Pressure-displacement behaviour for an example specimen is plotted in Figure 5 (a) and gives
247 a direct comparison of the change in behaviour over three cycles. All specimens exhibited
248 nonlinear pressure-displacement behaviour up to a pressure of between 20 and 30 mmHg.
249 Beyond this level of internal pressure, the behaviour became almost linear. Progression from

250 the first to second loading cycle exhibited a notable stiffness increase in all specimens of
251 $34\pm 10\%$ on average over the pressure range. A similar comparison between the second and
252 third cycles showed that the stiffness increase reduced to $5\pm 4\%$. Initial trials involving four
253 loading cycles yielded only a further $3\pm 4\%$ stiffness increase between the third and fourth
254 cycles, which justified the use of third cycle results as representative of the specimens'
255 repeatable behaviour. Displacements at the posterior pole for all specimens during the third
256 loading cycle ranged between 46 and 126 μm ($90\pm 26 \mu\text{m}$) at 16 mmHg up to between 116
257 and 220 μm ($191\pm 54 \mu\text{m}$) at 61 mmHg. Average behaviour observed during the third loading
258 cycle for all specimens is shown in Figure 5 (b).

259

260 Analysis of specimen deformation using DIC demonstrated a gradual reduction in posterior
261 displacement towards the equatorial region from a maximum at the posterior pole, Figure 6.
262 At the maximum pressure applied, displacement of the transverse plane (temporal-nasal
263 meridian) points positioned at 30° and 60° relative to the longitudinal axis were $155\pm 15\mu\text{m}$ and
264 $113\pm 17\mu\text{m}$, respectively. The corresponding points on the sagittal plane (superior-inferior)
265 meridian experienced similar displacements of $160\pm 15\mu\text{m}$ and $118\pm 19\mu\text{m}$.

266

267 **Numerical Results**

268 Following optimisation, the FE models demonstrated the same progressive increase in
269 posterior displacement that was evident in the specimens during the experimental stage of the
270 study, Figure 7. An example comparison of experimental displacements at the 9 points on
271 Specimen 5 at which displacements were monitored, and those produced by the
272 corresponding numerical model is shown in Figure 8. The comparison shows that model
273 predictions closely matched the experimental results. The average errors for all specimens at
274 the 9 points on the sclera when IOP was equal to 16, 31, 46 and 61mmHg were $8\pm 7\mu\text{m}$,
275 $8\pm 7\mu\text{m}$, $10\pm 8\mu\text{m}$, and $14\pm 10\mu\text{m}$, respectively.

276

277 The material parameters obtained for all specimens (see Table 1 in Appendix) were used to
278 enable comparisons between the tangent modulus values, as calculated from circumferential
279 stress-strain behaviour, in different regions relative to those around the posterior pole, Figure
280 9. The comparisons were held at four stress levels; 0.001, 0.005, 0.01 and 0.1 MPa, and it
281 was clear that under low stresses (up to 0.005 MPa) there was a gradual reduction in tissue
282 stiffness towards the posterior pole. For three of the five specimens, this reduction in stiffness
283 was statistically significant at the 0.01 level. However, as the stress levels increased, the
284 differences in stiffness between the six regions became gradually less apparent and
285 statistically insignificant. The average circumferential stress-strain and tangent modulus-
286 stress behaviour over the six regions for all specimens is presented in Figure 10.

287

288 **Discussion**

289 This study presents a novel method of optimising regional material properties capable of
290 replicating global displacements, as measured at nine target points, from experimental
291 inflation testing of human sclerae using 2D DIC and inverse FE modelling. Specimen-specific
292 FE meshes incorporating regional thickness and topography variations were constructed
293 using elements divided into six circumferential regions. Each region was assigned a first-order
294 Ogden constitutive material model, the parameters of which were optimised in order to
295 minimise RMS errors of pressure-displacement behaviour at locations in the FE models that
296 corresponded to the nine target points on the sclera surface. The maximum RMS error
297 between the experimental and numerical displacements within individual specimens was
298 17.5 μ m, demonstrating the ability of this method to obtain material behaviour parameters for
299 ophthalmology-related FE research studies where macroscale sclera displacements are
300 required.

301

302 The experimental protocol subjected human sclerae to cycles of internal pressure up to 61
303 mmHg to assess global displacements beyond the normal physiological and elevated
304 pressure ranges typically seen in glaucoma. The pressure-displacement behaviour observed

305 during the inflation tests closely matched the nonlinear behaviour observed in similar testing
306 scenarios for human (Fazio et al., 2012, Pyne et al., 2014, Tang et al., 2013, Woo et al., 1972),
307 monkey (Girard et al., 2009a, Girard et al., 2009b) and porcine (Girard et al., 2008) sclera.
308 Variations in pressure-displacement behaviour observed between different specimens could
309 be partly attributed to the age variation between donor specimens used in this study
310 (Coudrillier et al., 2015a).

311

312 All specimens demonstrated considerable thickness variation with maximum values in the
313 vicinity of the posterior pole, reducing to a minimum close to the equator before increasing
314 towards the anterior foramen. Similar to earlier studies (Elsheikh et al., 2010, Norman et al.,
315 2010), measurements along the orthogonal meridians demonstrated reduced thickness
316 compared to the diagonal meridians, however, all lines followed the same overall trend. The
317 biomechanical behaviour results show a consistent trend of gradual stiffness reduction from
318 the equator towards the posterior pole. While the trend was clear and statistically significant
319 ($P=0.01$) for the majority of specimens at low stresses up to 0.005 MPa, it became less
320 apparent and statistically insignificant under larger stresses for all specimens.

321

322 Various approaches have been used in inverse FE analyses of the posterior sclera. In a study
323 carried out by Woo et al. (1972), the sclera was modelled as a single set of isotropic elements
324 and their material behaviour was adjusted to fit a trilinear behaviour curve. In the work of Girard
325 et al. (2009c), the posterior sclera was divided into nine sub-regions. Four sub-regions were
326 orientated around the peripheral sclera, four around the parapapillary sclera and one around
327 the optic disc and preferred fibre orientations were optimised for each region. In the work of
328 Coudrillier et al. (2013), particular attention was given to the region spanning from the optic
329 nerve to the mid-peripheral sclera where specimen-specific information on collagen
330 orientations was obtained using WAXS. DIC-measured displacements were then applied as
331 kinematic boundary conditions around this region in their models. A more recent study by
332 Kollech et al. (2019) applied a different approach where sub-regions of the sclera were defined

333 based on first principal strains, as measured using sequential DIC. Inverse FE analysis was
334 then used to optimise Holzapfel anisotropic material parameters within each sub-region.

335

336 The aforementioned advances in ophthalmology-related inverse FE modelling have provided
337 valuable insights into the effects of scleral anisotropy (Coudrillier et al., 2013, Girard et al.,
338 2009b, Grytz et al., 2014a), age-related stiffening (Coudrillier et al., 2015a, Coudrillier et al.,
339 2012, Girard et al., 2009a), diabetes (Coudrillier et al., 2015b), race (Grytz et al., 2014b) and
340 chronic IOP elevation (Coudrillier et al., 2015c, Girard et al., 2011). The inclusion anisotropic
341 material properties are undoubtedly necessary for FE studies that aim to investigate the
342 mechanical response of the optic nerve head. While variations in the mechanical properties of
343 the lamina cribrosa have been shown to have little effect on the surrounding sclera (Girard et
344 al., 2009b), the removal of anisotropy from the peripapillary region can significantly affect the
345 behaviour of the sclera canal and lamina cribrosa (Coudrillier et al., 2013). However, in studies
346 where microscale sclera displacements are not required such as design optimisation of
347 ophthalmology-related medical devices or corneal studies where only global sclera
348 displacement behaviour is important, our methodology can be applied to obtain suitable
349 material parameters for use in FE models.

350

351 There are a number of limitations related to this study. Firstly, the same clamping mechanism
352 was used in all inflation tests. In addition to the fixed boundary conditions created by the
353 clamps, the use of a single clamp size coupled with the inter-specimen variation in sclera
354 diameter (24.26 ± 0.38 mm) would be expected to induce non-physiological stresses within the
355 adjacent tissue. While this impacted the overall posterior displacement of the sclera, a trial
356 carried out using FE analysis found the fixed boundary effects within the tissue to have
357 diminished by the specimen equator.

358

359 Secondly, the FE model was based on a number of assumptions which could have affected
360 the accuracy of its predictions. The division of the sclera into circumferential regions, although

361 justified by the approximately circumferential orientation of the displacement contour lines
362 (Figure 6), ignored possible variations in the scleral microstructure. A related limitation is the
363 assumption of isotropic sclera material behaviour in the FE models. This assumption, which
364 was necessary because of the same lack of information on scleral microstructure, was based
365 on a study in which the posterior sclera behaviour was found to be almost isotropic with the
366 average difference in stiffness between two orthogonal loading directions limited to 6%.

367

368 Thirdly, target curves used in the inverse modelling procedure were obtained from points along
369 the orthogonal meridians only. Consequently, and in contrast to studies that used fibre
370 reinforced models (Coudrillier et al., 2013, Coudrillier et al., 2012, Grytz et al., 2014a, Pyne et
371 al., 2014), the optimised material parameters presented in this study provide a means of
372 simulating whole hemisphere behaviour but may not represent more local behaviour at points
373 on the sclera shell between the meridians. Similarly, the finite element models were based on
374 the thickness measurements along the orthogonal and diagonal meridian lines, and
375 interpolation of thickness values was necessary for the areas between the meridian lines. It is
376 difficult to estimate the effect of this approximation on the model's predictions, but it is unlikely
377 to be significant. A further approximation was the simple and standard form assumed for the
378 lamina cribrosa, which was necessary due to our inability to distinguish between the nerve
379 fibres and scleral tissue and to measure the dimensions of the lamina cribrosa. While these
380 limitations, combined, are expected to have an effect on the FE predictions of the distribution
381 of stress, strain and deformation, they are unlikely to have a notable effect on overall
382 behaviour.

383

384 Finally, the loading regime adopted in this study was similar to those followed by other
385 researchers (Danielsen, 2004, Girard et al., 2009a, Schultz et al., 2008, Zeng et al., 2001)
386 where no recovery was included between the conditioning cycles and the specimens were not
387 allowed to creep before the final loading cycle. However, it is recognised that other studies
388 introduced different loading regimes incorporating recovery and creep and this could have an

389 effect on the obtained behaviour (Boyce et al., 2008). In particular, it has been argued that
390 without recovery time the behaviour is likely to be affected by the strain history of
391 preconditioning cycles (Carew et al., 2000). In appreciation of the potential importance of these
392 effects, further tests will be conducted in which variations in the loading regime, including
393 protocols to assess viscoelasticity, will be introduced to assess their effect on the obtained
394 behaviour.

395

396 **Conclusion**

397 The study demonstrated how inflation testing combined with inverse modelling could be used
398 to effectively characterise regional material properties of ocular tissue using circumferential
399 regions of isotropic elements to replicate macroscale sclera displacements. The material
400 properties were found to vary between specimens, and it is expected that age could be a
401 contributing factor behind this variation. While this study laid out the experimental and inverse
402 modelling procedures and presented overall behaviour patterns, follow up studies will attempt
403 to characterise the variation in properties of scleral tissue with age and medical history.

404 **References**

- 405 ALASTRUE, V., CALVO, B., PENA, E. & DOBLARE, M. 2006. Biomechanical modeling of
406 refractive corneal surgery. *J Biomech Eng*, 128, 150-60.
- 407 BATTAGLIOLI, J. L. & KAMM, R. D. 1984. Measurements of the compressive properties of
408 scleral tissue. *Investigative Ophthalmology and Visual Science*, 25, 59-65.
- 409 BOYCE, B. L., GRAZIER, J. M., JONES, R. E. & NGUYEN, T. D. 2008. Full-field deformation
410 of bovine cornea under constrained inflation conditions. *Biomaterials*, 29, 3896-3904.
- 411 CAREW, E. O., BARBER, J. E. & VESELY, I. 2000. Role of preconditioning and recovery time
412 in repeated testing of aortic valve tissues: validation through quasilinear viscoelastic
413 theory. *Ann Biomed Eng*, 28, 1093-100.
- 414 COUDRILLIER, B., BOOTE, C., QUIGLEY, H. A. & NGUYEN, T. D. 2013. Scleral anisotropy
415 and its effects on the mechanical response of the optic nerve head. *Biomechanics and
416 Modeling in Mechanobiology*, 12, 941-963.
- 417 COUDRILLIER, B., PIJANKA, J., JEFFERYYS, J., SORENSEN, T., QUIGLEY, H. A., BOOTE,
418 C. & NGUYEN, T. D. 2015a. Collagen Structure and Mechanical Properties of the
419 Human Sclera: Analysis for the Effects of Age. *Journal of Biomechanical Engineering*,
420 137.
- 421 COUDRILLIER, B., PIJANKA, J., JEFFERYYS, J., SORENSEN, T., QUIGLEY, H. A., BOOTE,
422 C. & NGUYEN, T. D. 2015b. Effects of age and diabetes on scleral stiffness. *Journal
423 of Biomechanical Engineering*, 137.
- 424 COUDRILLIER, B., PIJANKA, J. K., JEFFERYYS, J. L., GOEL, A., QUIGLEY, H. A., BOOTE,
425 C. & NGUYEN, T. D. 2015c. Glaucoma-related changes in the mechanical properties
426 and collagen micro-architecture of the human sclera. *PLoS ONE*, 10.
- 427 COUDRILLIER, B., TIAN, J., ALEXANDER, S., MYERS, K. M., QUIGLEY, H. A. & NGUYEN,
428 T. D. 2012. Biomechanics of the human posterior sclera: Age- and glaucoma-related
429 changes measured using inflation testing. *Investigative Ophthalmology and Visual
430 Science*, 53, 1714-1728.
- 431 DANIELSEN, C. C. 2004. Tensile mechanical and creep properties of Descemet's membrane
432 and lens capsule. *Exp Eye Res*, 79, 343-50.
- 433 DOWNS, J. C., SUH, J. K., THOMAS, K. A., BELLEZZA, A. J., BURGOYNE, C. F. & HART,
434 R. T. 2003. Viscoelastic characterization of peripapillary sclera: material properties by
435 quadrant in rabbit and monkey eyes. *J Biomech Eng*, 125, 124-31.
- 436 EILAGHI, A., FLANAGAN, J. G., SIMMONS, C. A. & ETHIER, C. R. 2010. Effects of scleral
437 stiffness properties on optic nerve head biomechanics. *Annals of biomedical
438 engineering*, 38, 1586-1592.
- 439 ELSHEIKH, A., GERAGHTY, B., ALHASSO, D., KNAPPETT, J., CAMPANELLI, M. & RAMA,
440 P. 2010. Regional variation in the biomechanical properties of the human sclera.
441 *Experimental Eye Research*, 90, 624-633.
- 442 ELSHEIKH, A. & WANG, D. 2007. Numerical modelling of corneal biomechanical behaviour.
443 *Comput Methods Biomech Biomed Engin*, 10, 85-95.
- 444 ELSHEIKH, A., WANG, D., BROWN, M., RAMA, P., CAMPANELLI, M. & PYE, D. 2007.
445 Assessment of corneal biomechanical properties and their variation with age. *Current
446 Eye Research*, 32, 11-19.
- 447 FAZIO, M. A., GRYZT, R., BRUNO, L., GIRARD, M. J. A., GARDINER, S., GIRKIN, C. A. &
448 DOWNS, J. C. 2012. Regional variations in mechanical strain in the posterior human
449 sclera. *Investigative Ophthalmology and Visual Science*, 53, 5326-5333.
- 450 FERNANDEZ, D. C., NIAZY, A. M., KURTZ, R. M., DJOTYAN, G. P. & JUHASZ, T. 2006. A
451 finite element model for ultrafast laser-lamellar keratoplasty. *Ann Biomed Eng*, 34, 169-
452 83.
- 453 GEFEN, A., SHALOM, R., ELAD, D. & MANDEL, Y. 2009. Biomechanical analysis of the
454 keratoconic cornea. *Journal of the Mechanical Behavior of Biomedical Materials*, 2,
455 224-236.

456 GERAGHTY, B., JONES, S. W., RAMA, P., AKHTAR, R. & ELSHEIKH, A. 2012. Age-related
457 variations in the biomechanical properties of human sclera. *Journal of the Mechanical*
458 *Behavior of Biomedical Materials*, 16, 181-191.

459 GIRARD, M. J., DOWNS, J. C., BURGOYNE, C. F. & SUH, J. K. 2008. Experimental surface
460 strain mapping of porcine peripapillary sclera due to elevations of intraocular pressure.
461 *J Biomech Eng*, 130, 041017.

462 GIRARD, M. J., SUH, J. K., BOTTLANG, M., BURGOYNE, C. F. & DOWNS, J. C. 2009a.
463 Scleral Biomechanics in the Aging Monkey Eye. *Invest Ophthalmol Vis Sci*.

464 GIRARD, M. J. A., DOWNS, J. C., BOTTLANG, M., BURGOYNE, C. F. & SUH, J. K. F. 2009b.
465 Peripapillary and posterior scleral mechanics - Part II: Experimental and inverse finite
466 element characterization. *Journal of Biomechanical Engineering*, 131.

467 GIRARD, M. J. A., DOWNS, J. C., BURGOYNE, C. F. & SUH, J. K. F. 2009c. Peripapillary
468 and posterior scleral mechanics - Part I: Development of an anisotropic hyperelastic
469 constitutive model. *Journal of Biomechanical Engineering*, 131.

470 GIRARD, M. J. A., FRANCIS SUH, J. K., BOTTLANG, M., BURGOYNE, C. F. & CRAWFORD
471 DOWNS, J. 2011. Biomechanical changes in the sclera of monkey eyes exposed to
472 chronic IOP elevations. *Investigative Ophthalmology and Visual Science*, 52, 5656-
473 5669.

474 GRYTZ, R., FAZIO, M. A., GIRARD, M. J. A., LIBERTIAUX, V., BRUNO, L., GARDINER, S.,
475 GIRKIN, C. A. & CRAWFORD DOWNS, J. 2014a. Material properties of the posterior
476 human sclera. *Journal of the Mechanical Behavior of Biomedical Materials*, 29, 602-
477 617.

478 GRYTZ, R., FAZIO, M. A., LIBERTIAUX, V., BRUNO, L., GARDINER, S., GIRKIN, C. A. &
479 DOWNS, J. C. 2014b. Age-and race-related differences in human scleral material
480 properties. *Investigative Ophthalmology and Visual Science*, 55, 8163-8172.

481 GRYTZ, R. & MESCHKE, G. 2010. A computational remodeling approach to predict the
482 physiological architecture of the collagen fibril network in corneo-scleral shells.
483 *Biomechanics and Modeling in Mechanobiology*, 9, 225-235.

484 KOLLECH, H. G., AYYALASOMAYAJULA, A., BEHKAM, R., TAMIMI, E., FURDELLA, K.,
485 DREWRY, M. & GEEST, J. P. V. 2019. A subdomain method for mapping the
486 heterogeneous mechanical properties of the human posterior Sclera. *Frontiers in*
487 *Bioengineering and Biotechnology*, 7.

488 NORMAN, R. E., FLANAGAN, J. G., RAUSCH, S. M. K., SIGAL, I. A., TERTINEGG, I.,
489 EILAGHI, A., PORTNOY, S., SLED, J. G. & ETHIER, C. R. 2010. Dimensions of the
490 human sclera: Thickness measurement and regional changes with axial length.
491 *Experimental Eye Research*, 90, 277-284.

492 PYNE, J. D., GENOVESE, K., CASALETTO, L. & GEEST, J. P. V. 2014. Sequential-digital
493 image correlation for mapping human posterior sclera and optic nerve head
494 deformation. *Journal of Biomechanical Engineering*, 136.

495 QUEIRÓS, A., GONZÁLEZ-MÉIJOME, J. M., FERNANDES, P., JORGE, J., ALMEIDA, J. B.
496 & PARAFITA, M. A. 2007. Technical note: Accuracy and repeatability of a new portable
497 ultrasound pachymeter. *Ophthalmic and Physiological Optics*, 27, 190-193.

498 SAUDE, T. 1993. *Ocular Anatomy and Physiology*, London, Wiley-Blackwell.

499 SCHULTZ, D. S., LOTZ, J. C., LEE, S. M., TRINIDAD, M. L. & STEWART, J. M. 2008.
500 Structural factors that mediate scleral stiffness. *Invest Ophthalmol Vis Sci*, 49, 4232-6.

501 SIGAL, I. A. 2009. Interactions between geometry and mechanical properties on the optic
502 nerve head. *Invest Ophthalmol Vis Sci*, 50, 2785-95.

503 SIGAL, I. A., FLANAGAN, J. G. & ETHIER, C. R. 2005. Factors influencing optic nerve head
504 biomechanics. *Investigative Ophthalmology and Visual Science*, 46, 4189-4199.

505 TANG, J., HART, R., ROBERTS, C., WEBER, P., PAN, X. & LIU, J. 2013. Regional variation
506 of scleral strains measured on human whole globes using ultrasound speckle tracking.
507 *Invest. Ophthalmol. Vis. Sci.*, 54, 54-.

508 UCHIO, E., OHNO, S., KUDOH, J., AOKI, K. & KISIELEWICZ, L. T. 1999. Simulation model
509 of an eyeball based on finite element analysis on a supercomputer. *Br J Ophthalmol*,
510 83, 1106-11.

511 WOO, S. L., KOBAYASHI, A. S., SCHLEGEL, W. A. & LAWRENCE, C. 1972. Nonlinear
512 material properties of intact cornea and sclera. *Exp Eye Res*, 14, 29-39.
513 ZENG, Y., YANG, J., HUANG, K., LEE, Z. & LEE, X. 2001. A comparison of biomechanical
514 properties between human and porcine cornea. *J Biomech*, 34, 533-7.
515 ZHOU, D., ABASS, A., ELIASY, A., STUDER, H. P., MOVCHAN, A., MOVCHAN, N. &
516 ELSHEIKH, A. 2019. Microstructure-based numerical simulation of the mechanical
517 behaviour of ocular tissue. *Journal of the Royal Society Interface*, 16.
518

519

520 **Figure Captions**

521 Figure 1 (a) and (b) Schematic elevations of a sclera including (a) a view of specimen
522 orientation from the anterior side after cornea removal, and (b) a view of specimen dimensions
523 from the temporal side. Circular points = approximate locations of eye bank thickness
524 measurements. (c) and (d) Schematic elevations of sclera wall thickness measurement
525 locations obtained along eight meridians lines between the anterior foramen and posterior
526 pole, including (c) a view from the temporal side, and (d) a view from the posterior side. PP =
527 Posterior Pole, ON = Optic Nerve.

528

529 Figure 2 (a) Temporal view of a schematic cross-section through a clamped sclera showing
530 direction of the laser displacement sensor, and (b) posterior view of the sclera showing the
531 camera positions whereby camera 1 monitors the temporal-nasal meridian and camera 2
532 monitors the superior-inferior meridian. (c) and (d) Schematic elevations of sclera illustrating
533 the numbered points at which posterior displacements were monitored, including (c) a view
534 from the temporal side, and (d) a view from the posterior side. PP = Posterior Pole. ON = Optic
535 Nerve.

536

537 Figure 3 (a) Nasal and (b) posterior illustration of the finite element mesh showing the six
538 element groups used during the inverse modelling procedure. ONH = Optic Nerve Head

539

540 Figure 4 Contour map of thickness variation at 25 μm intervals on a developed scleral surface
541 for (a) average data obtained from all sclerae tested, and (b) represents the locations of
542 thickness measurements. Colour bar values are presented in micrometres (μm). The map
543 centre represents the posterior pole. Maps continue to the anterior foramen edge. S = superior
544 direction, I = inferior direction, N = nasal direction, T = temporal direction, ONH = optic nerve
545 head.

546 Figure 5 Example pressure-displacement behaviour measured at the posterior pole for (a) a
547 58 year old donor specimen over three cycles (plotted from a point of zero displacement to
548 allow direct comparison between cycles) and (b) average pressure-displacement behaviour
549 during the third loading for all specimens.

550

551 Figure 6 Contour maps of posterior displacements in millimetres observed experimentally from
552 camera 1 (superior view) for a 58 year old donor specimen.

553

554 Figure 7 Example of FE model-predicted posterior displacements in millimetres over the sclera
555 surface for a 58 year old donor specimen. Reduced thickness section on left side of model
556 represents the location of the lamina cribrosa.

557

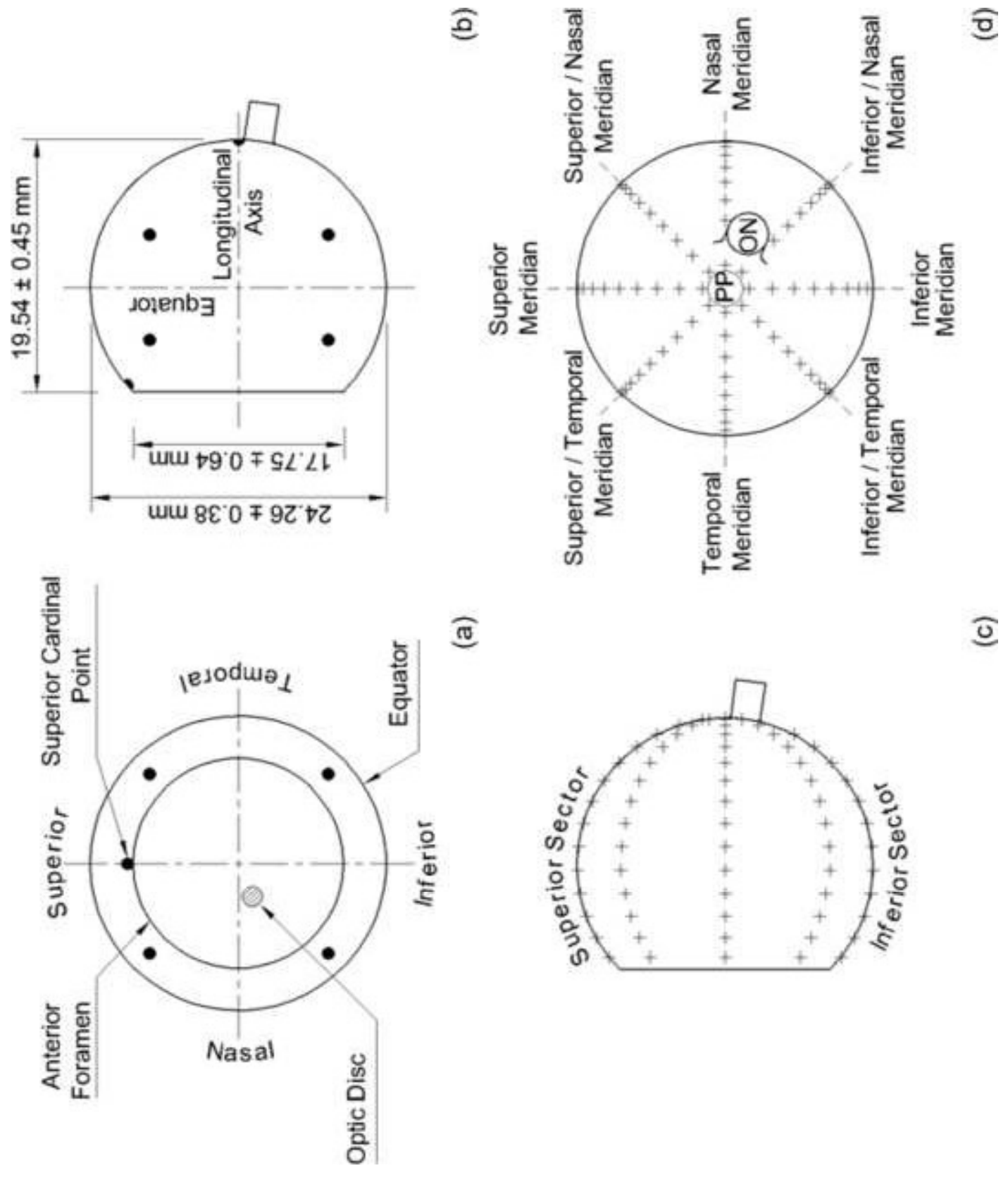
558 Figure 8 Example of fit between experimental and numerical posterior displacements for a 58
559 year old donor (Specimen 5), obtained at the monitored points shown in Figure 2 (c) and (d)
560 on the sclera surface.

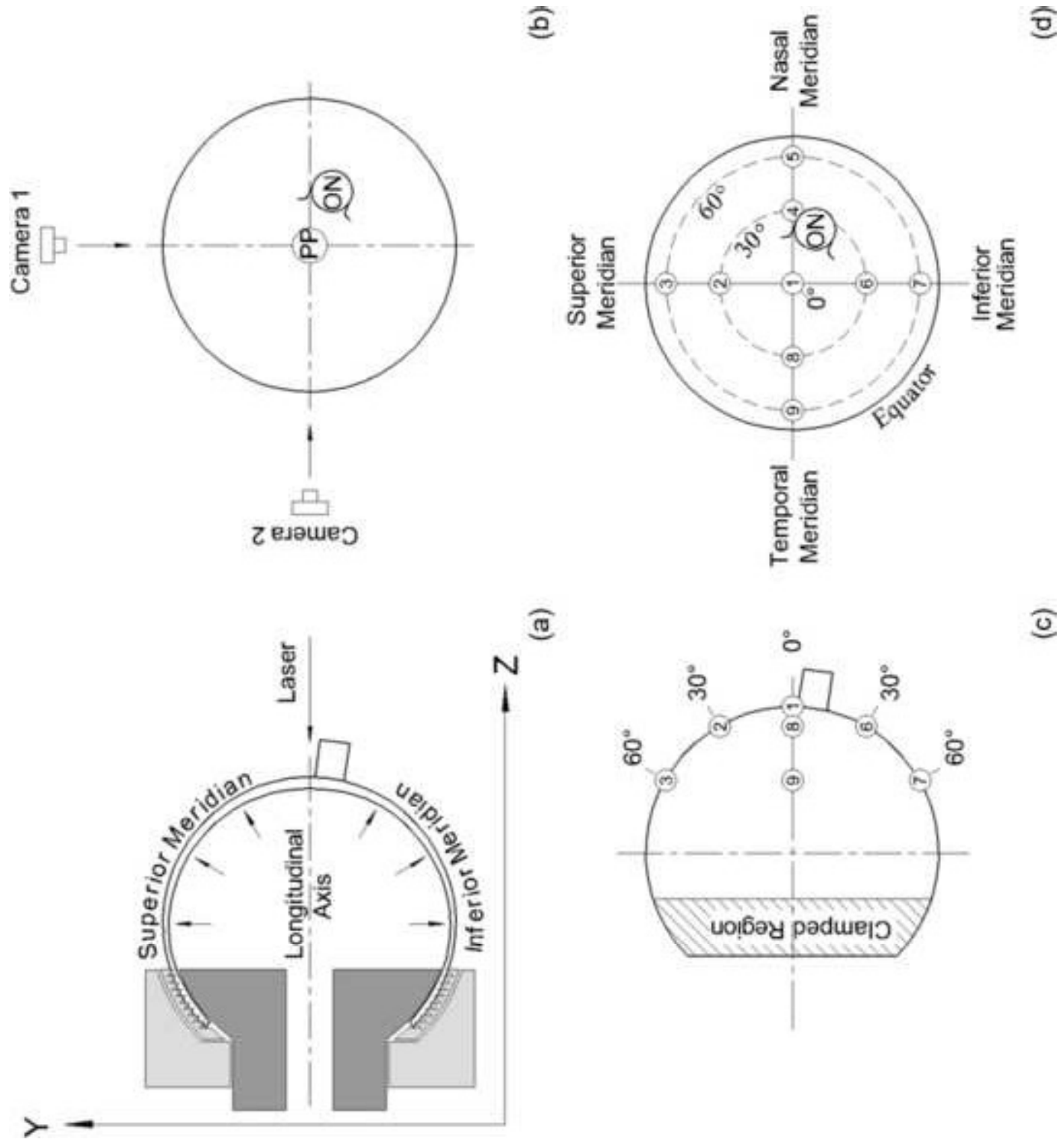
561

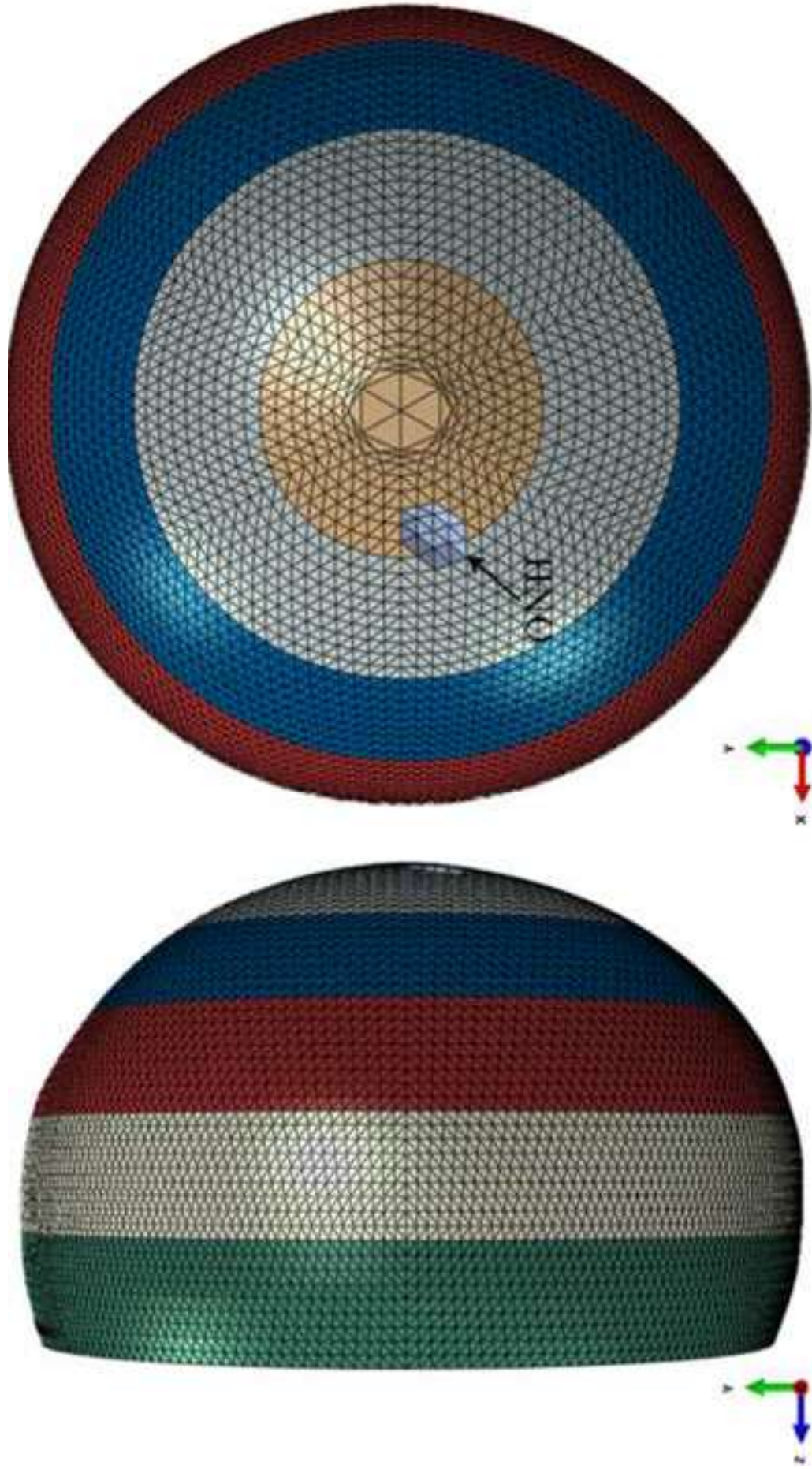
562 Figure 9 Ratios for tangent modulus within each region (R1 to R6) of the sclera models relative
563 to tangent modulus at the posterior pole (R6) when stress is equal to (a) 0.001 MPa, (b) 0.005
564 MPa, (c) 0.01 MPa, and (d) 0.1 MPa.

565

566 Figure 10 Average behaviour in the circumferential direction for each sclera showing (a)
567 stress-strain and (b) tangent modulus-stress trends for the six regions. Error bars represent
568 standard deviation.

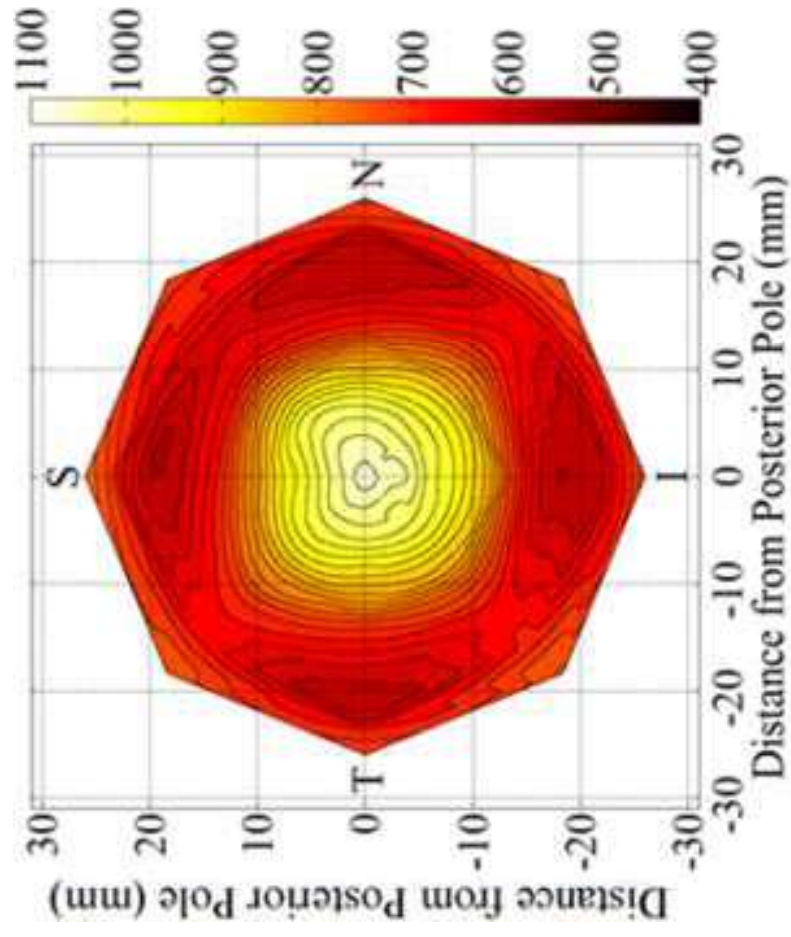




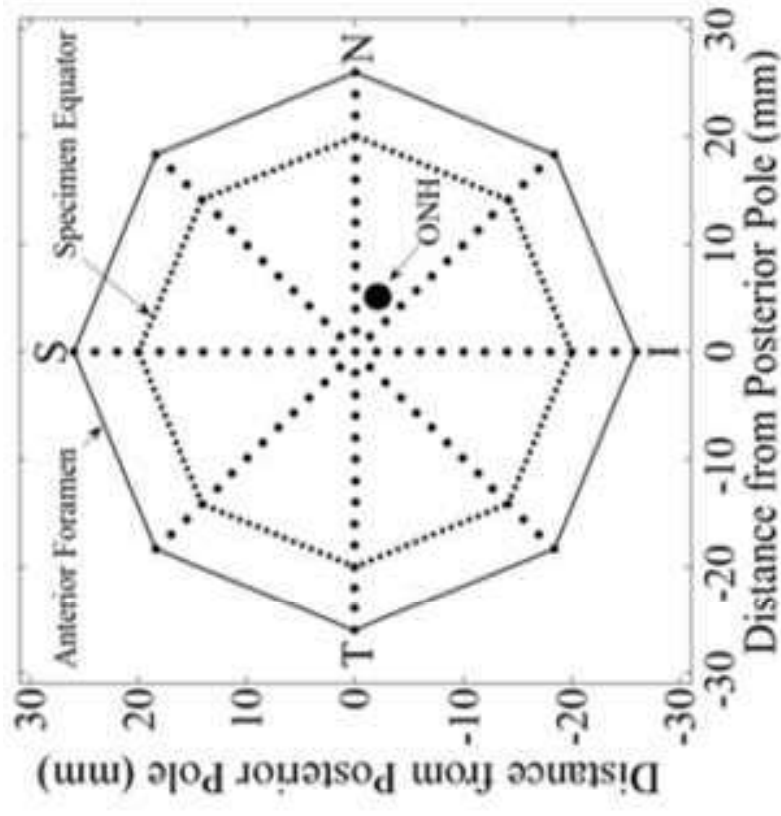


(a)

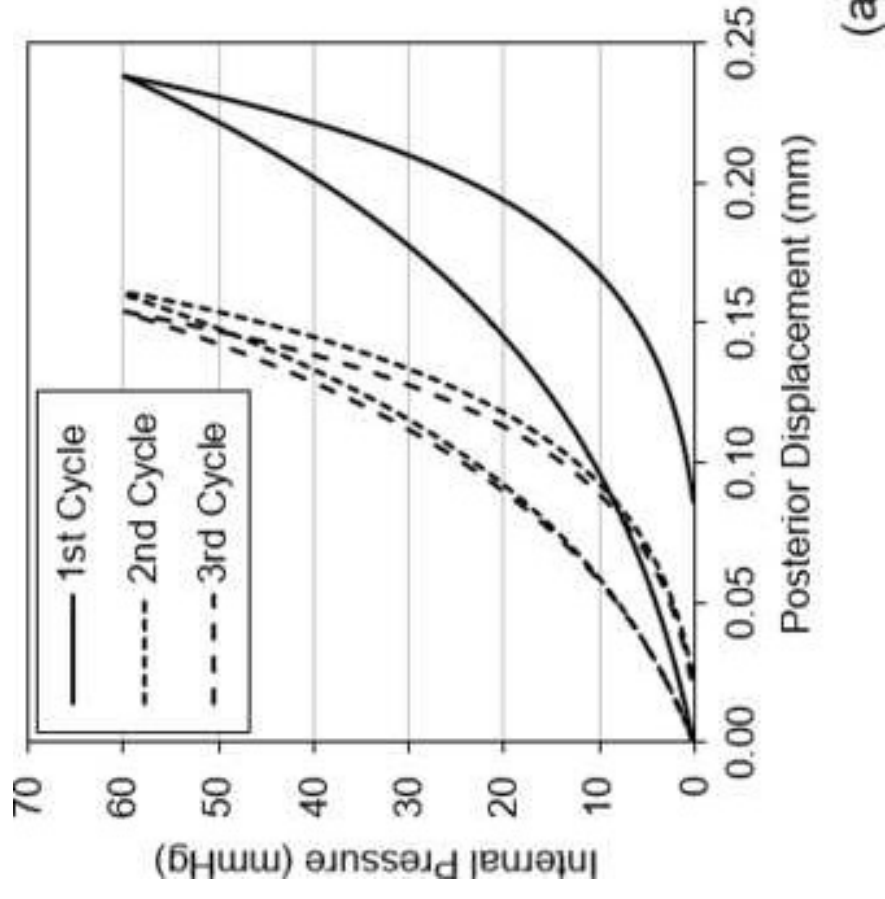
(b)



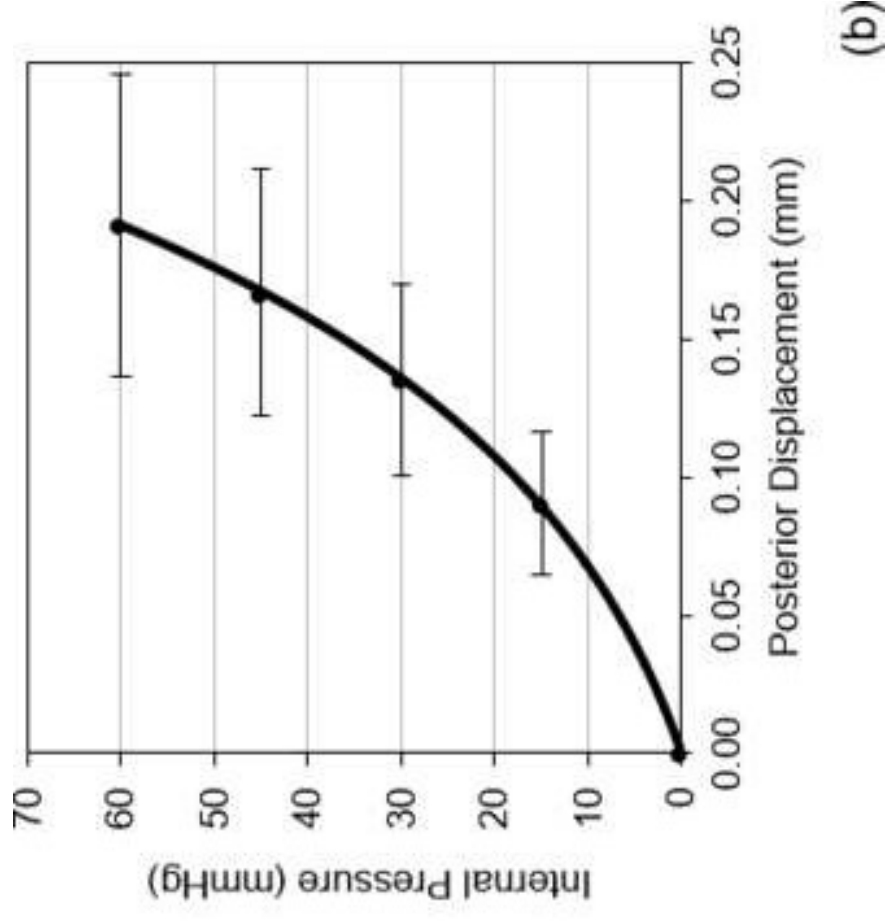
(a)



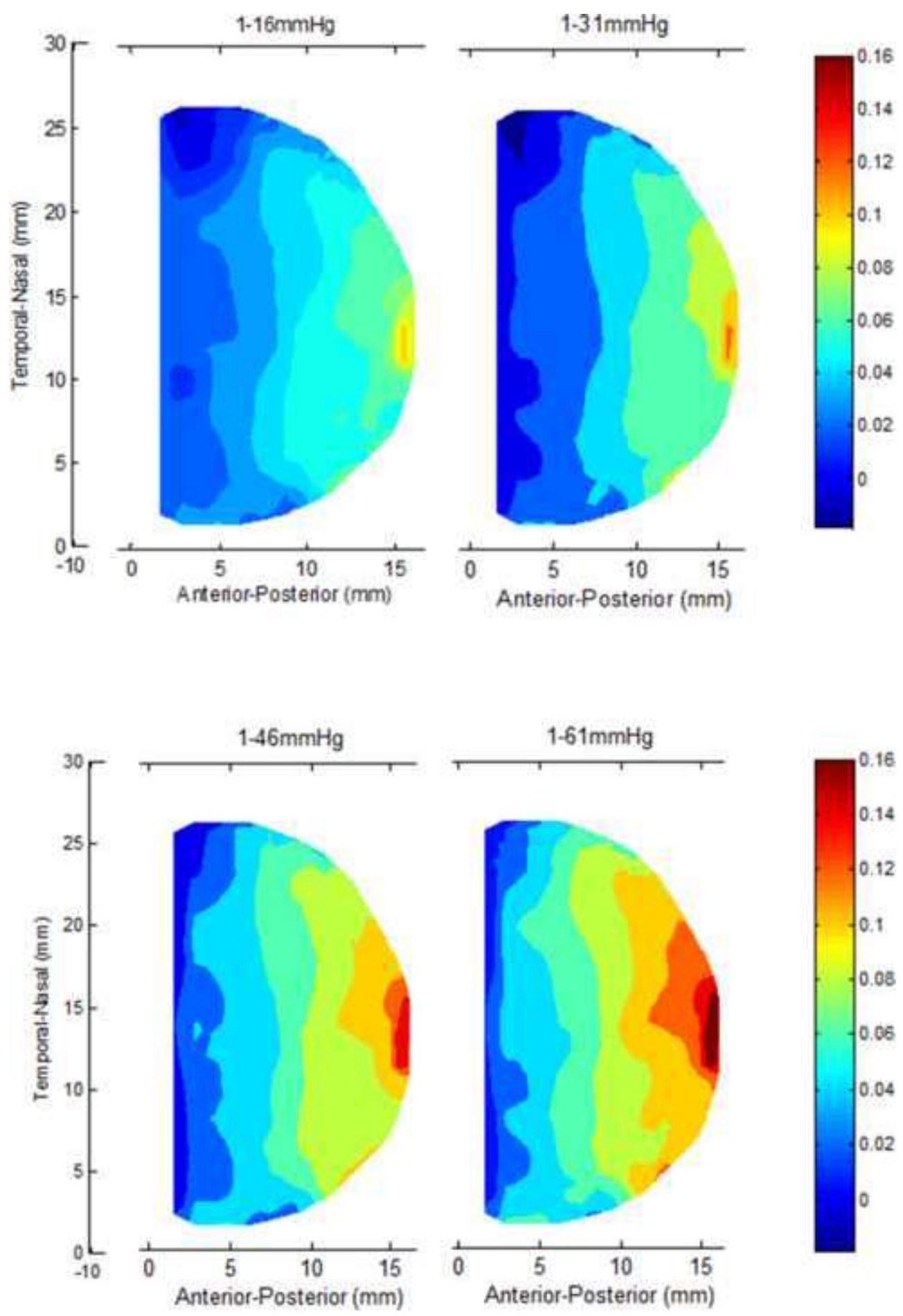
(b)

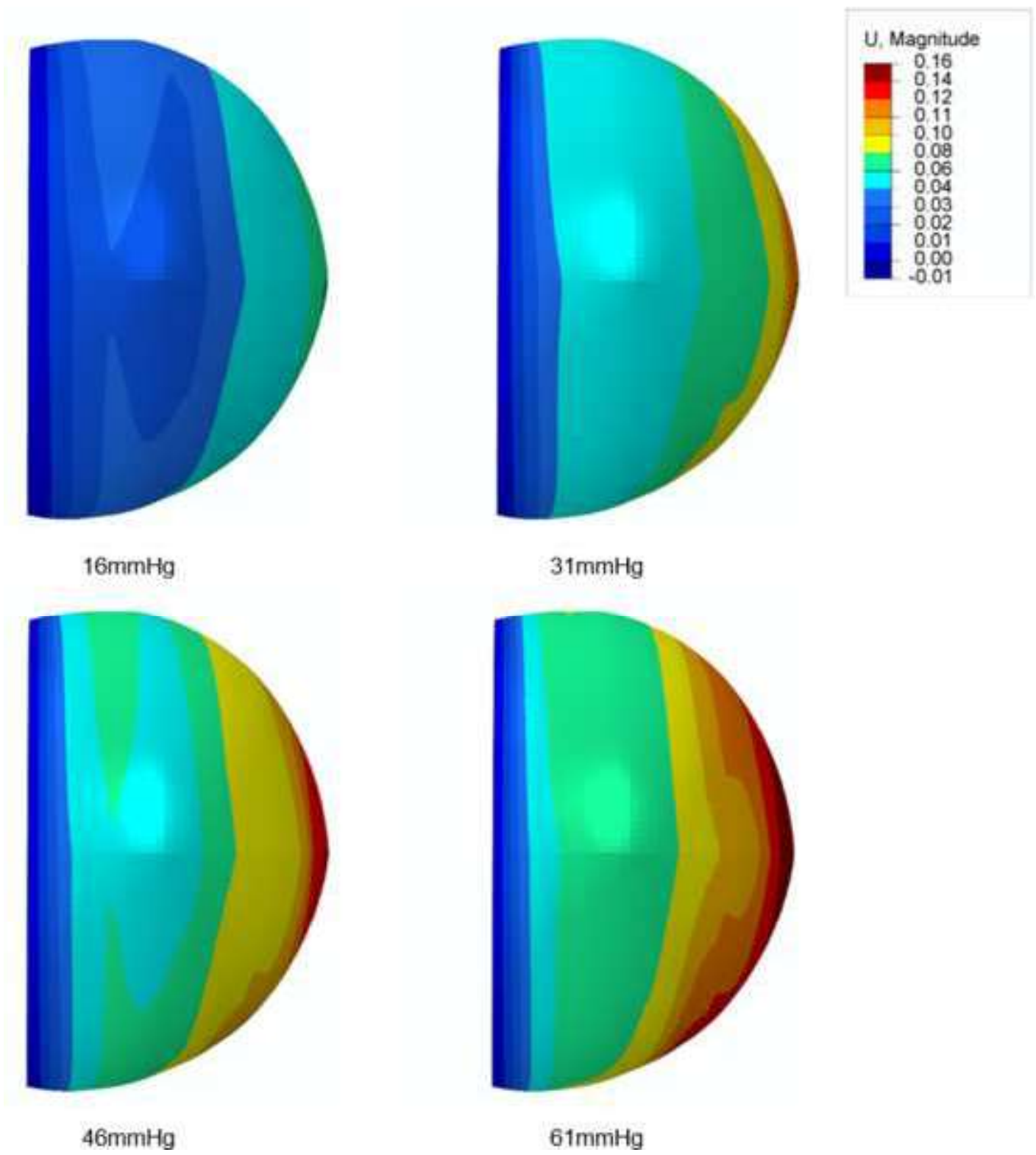


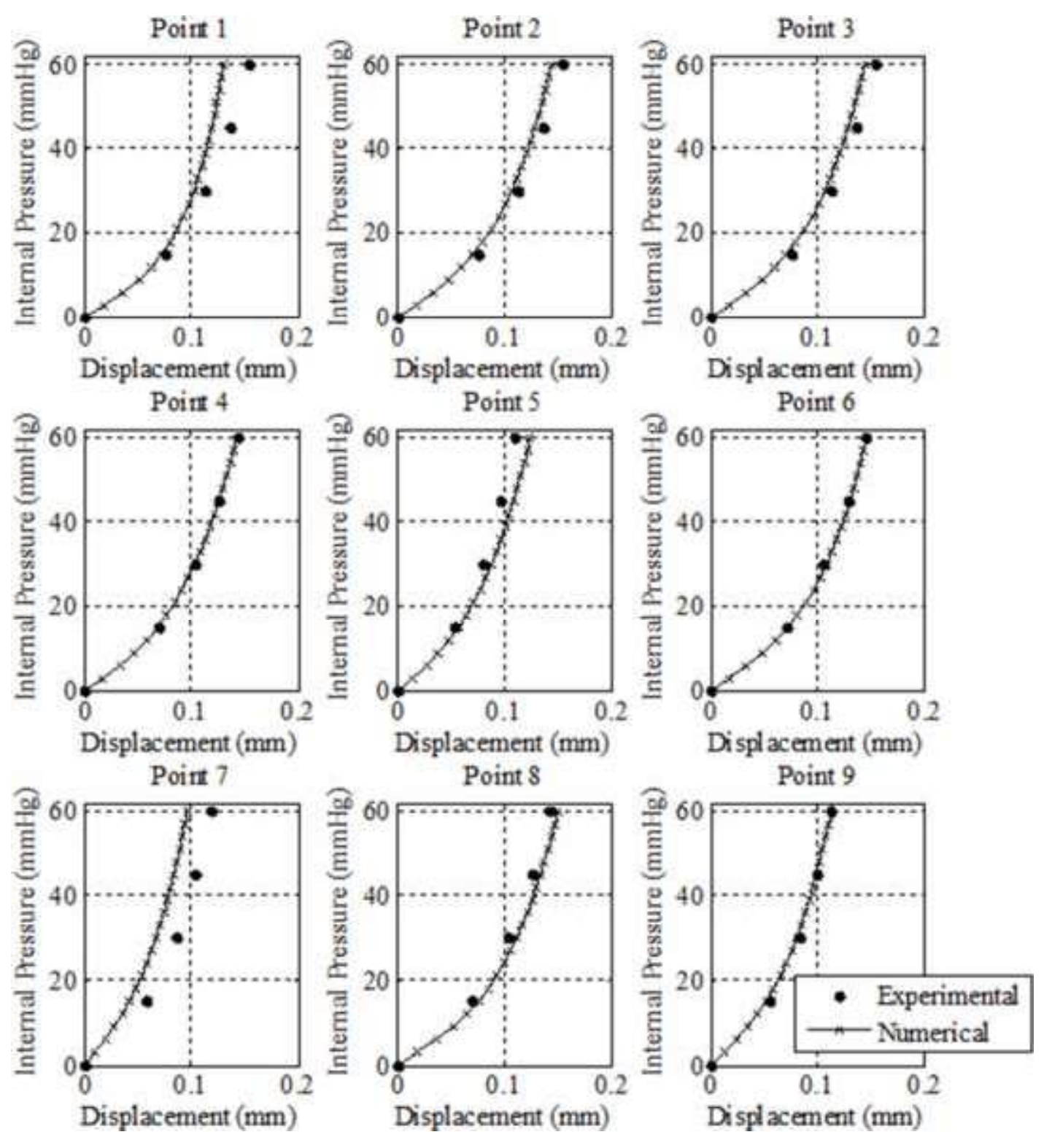
(a)

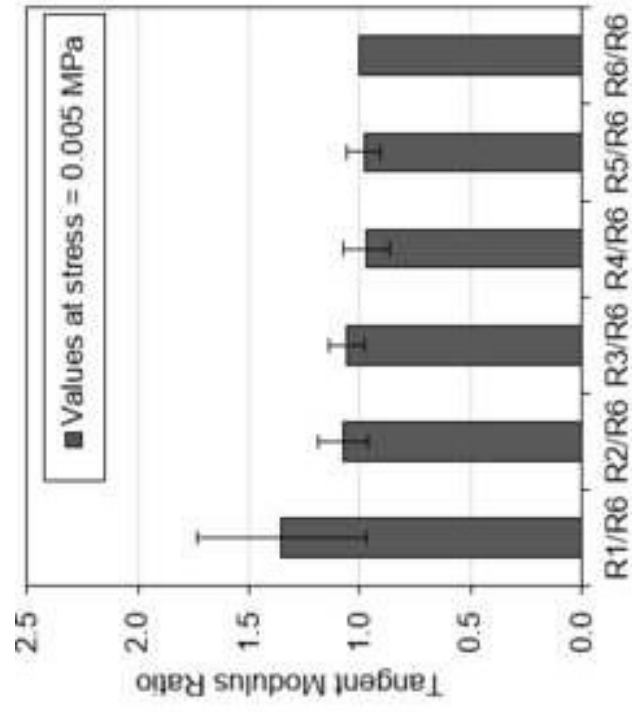


(b)

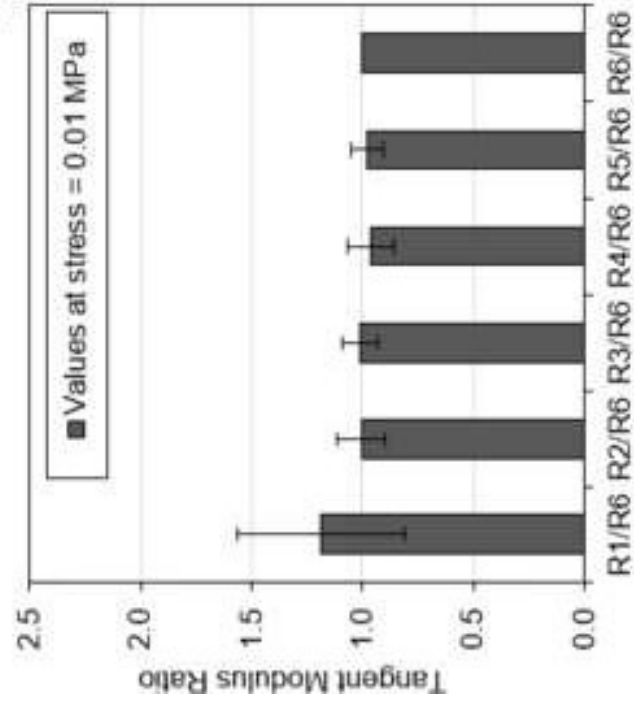




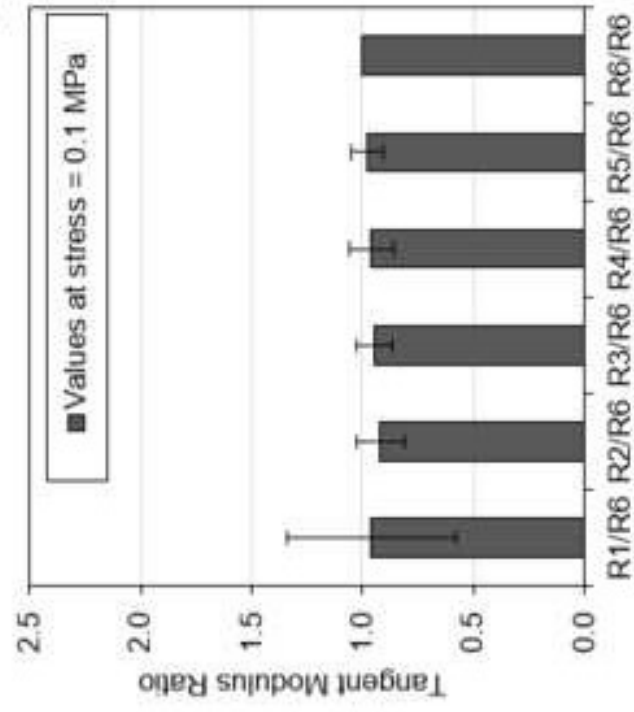




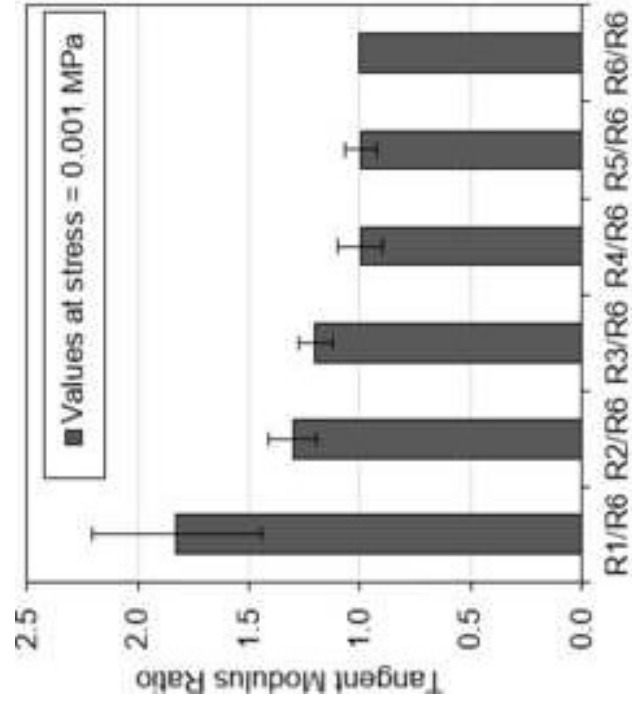
(a)



(b)



(c)



(d)

